

# PCCP

Accepted Manuscript



This is an *Accepted Manuscript*, which has been through the Royal Society of Chemistry peer review process and has been accepted for publication.

*Accepted Manuscripts* are published online shortly after acceptance, before technical editing, formatting and proof reading. Using this free service, authors can make their results available to the community, in citable form, before we publish the edited article. We will replace this *Accepted Manuscript* with the edited and formatted *Advance Article* as soon as it is available.

You can find more information about *Accepted Manuscripts* in the [Information for Authors](#).

Please note that technical editing may introduce minor changes to the text and/or graphics, which may alter content. The journal's standard [Terms & Conditions](#) and the [Ethical guidelines](#) still apply. In no event shall the Royal Society of Chemistry be held responsible for any errors or omissions in this *Accepted Manuscript* or any consequences arising from the use of any information it contains.

# Nuclear Dynamics in the Metastable Phase of the Solid Acid Caesium Hydrogen Sulfate<sup>†</sup>

Maciej Krzystyniak,<sup>a,b</sup> Kacper Drużbicki,<sup>c,d</sup> and Felix Fernandez-Alonso<sup>a,e</sup>

Received Xth XXXXXXXXXXXX 20XX, Accepted Xth XXXXXXXXXXXX 20XX

First published on the web Xth XXXXXXXXXXXX 200X

DOI: 10.1039/XXXXXXXXXX

High-resolution spectroscopic measurements using thermal and epithermal neutrons and first-principles calculations within the framework of density-functional theory are used to investigate the nuclear dynamics of light and heavy species in the metastable phase of caesium hydrogen sulfate. Within the generalised-gradient approximation, extensive calculations show that both ‘standard’ and ‘hard’ formulations of the Perdew-Burke-Ernzerhof functional supplemented by Tkatchenko-Scheffler dispersion corrections provide an excellent description of the known structure, underlying vibrational density of states, and nuclear momentum distributions measured at 10 and 300 K. Encouraged by the agreement between experiment and computational predictions, we provide a quantitative appraisal of the quantum contributions to nuclear motions in this solid acid. From this analysis, we find that only the heavier caesium atoms reach the classical limit at room temperature. Contrary to naïve expectation, sulfur exhibits a more pronounced quantum character relative to classical predictions than the lighter oxygen atom. We interpret this hitherto unexplored nuclear quantum effect as arising from the tighter binding environment of this species in this technologically relevant material.

## 1 Introduction

At ambient pressure, the solid acid caesium hydrogen sulfate (hereafter CsHSO<sub>4</sub>) exhibits three crystalline phases, namely, phase III below ~330-370 K, phase II up to ~410-415 K, and phase I at higher temperatures.<sup>1-3</sup> Both phases III and II are monoclinic (space group *P2*<sub>1</sub>/*c*), and phase I is tetragonal (space group *I4*<sub>1</sub>/*amd*). This lower-symmetry phase exhibits an outstanding bulk ionic conductivity of ~10<sup>-2</sup> Ω<sup>-1</sup>cm<sup>-1</sup>, a value that approaches those typical of ionic liquids.<sup>4</sup> The properties of CsHSO<sub>4</sub> phase I have already been exploited as the solid electrolyte in intermediate-temperature fuel cells operating up to ~500 K.<sup>5</sup> To date, a considerable body of work has been devoted to explore and understand the microscopic mechanism of proton conductivity in CsHSO<sub>4</sub> phase I, as well as the tetragonal-to-monoclinic phase transition to phase II. These include experimental studies on protonated (CsHSO<sub>4</sub>) and deuterated (CsDSO<sub>4</sub>) species using X-ray<sup>6-8</sup> and neu-

tron diffraction,<sup>9-11</sup> inelastic neutron scattering (INS),<sup>2,12-15</sup> optical spectroscopy,<sup>16-18</sup> and nuclear-magnetic resonance (NMR).<sup>19-21</sup> Likewise, CsHSO<sub>4</sub> phase I has been studied by molecular-dynamics (MD) simulations using force-field-based<sup>22,23</sup> and, more recently, first-principles<sup>24-26</sup> methodologies. In contrast, the properties of CsHSO<sub>4</sub> phases II and III below ~400 K have received far less attention than phase I. Room-temperature structures have been reported by Chisholm and Haile<sup>27</sup> and by Itoh *et al.*<sup>7</sup> for phases II and III, respectively. In a more recent study, Uda *et al.*<sup>28</sup> have extended these studies to investigate the thermal expansion of phases I, II, and III over the range 290-440 K.

CsHSO<sub>4</sub> phase III is an interesting material in its own right, as its very existence constitutes a unique occurrence amongst all solid acids of stoichiometry MHXO<sub>4</sub>, where M represents an alkali metal and X a chalcogen.<sup>29</sup> Although this phase is known to exist down to cryogenic temperatures, it is also metastable and can only be obtained when grown from an aqueous medium at room temperature.<sup>2,27,28</sup> Heating phase III to 330-370 K leads to an irreversible transformation to phase II, a process which results in a 0.6% volume *contraction* accompanied by a rather counter-intuitive *weakening* of hydrogen bonds linking SO<sub>4</sub> tetrahedra.<sup>28</sup> The precise transition temperature for this process is quite sensitive to crystallite size, surface composition of grains, level of humidity, and heating rate.<sup>2,30-33</sup> Also, crystallization in a deuterated aqueous solution with a deuterium-to-hydrogen molar content greater than 50% leads to the complete suppression of phase

<sup>†</sup> Electronic Supplementary Information (ESI) available. See DOI: 10.1039/XXXXXXXXXX/

<sup>a</sup> ISIS Facility, Rutherford Appleton Laboratory, Chilton, Didcot, Oxfordshire OX11 0QX, United Kingdom.

<sup>b</sup> School of Science and Technology, Nottingham Trent University, Clifton Campus, Nottingham, NG11 8NS, United Kingdom.

<sup>c</sup> Faculty of Physics, Adam Mickiewicz University, Umultowska St. 85, 61-614 Poznan, Poland.

<sup>d</sup> Frank Laboratory of Neutron Physics, Joint Institute for Nuclear Research, 141980, Dubna, Russian Federation.

<sup>e</sup> Department of Physics and Astronomy, University College London, Gower Street, London, WC1E 6BT, United Kingdom.

III in favour of phase II, an intriguing isotope effect whose underlying physico-chemical basis remains to be understood. Given the predominance of intermolecular hydrogen-bonding (HB) motifs in this material, such drastic changes upon isotopic substitution may be viewed as an extreme case of the Ubbelohde effect,<sup>34,35</sup> where HB elongation in the deuterated case is sufficient to prevent the formation of this phase. This behaviour is to be contrasted with the well-known insensitivity to deuteration of the transition temperature between phases II and I at 414 K (CsHSO<sub>4</sub>) and 412 K (CsDSO<sub>4</sub>), and a nearly identical activation enthalpy for ionic conduction of 0.26 (CsHSO<sub>4</sub>) and 0.27 eV (CsDSO<sub>4</sub>) in phase I. Both of these observations are indicative of a predominantly passive role played by the light species in driving the onset of superionic conductivity, in spite of a marked (positive) Ubbelohde effect upon deuteration of CsHSO<sub>4</sub> phase I. In this case, the O···O distance associated with the hydrogen bond expands from 2.57 Å (CsHSO<sub>4</sub>) to 2.64 Å (CsDSO<sub>4</sub>).<sup>29</sup> Surprisingly, no measurable change in O···O distances is observed between these two isotopomers in phase II.<sup>27</sup>

In view of the available phenomenology of CsHSO<sub>4</sub> phase III reviewed above, this work seeks to provide a sound description of the dynamics of atomic motions in this material. Such a task is facilitated by the absence of disorder in this particular phase and, therefore, represents a first and necessary step before attempting to tackle the more complex dynamical behaviour seen in the superionic phase of CsHSO<sub>4</sub> at higher temperatures. To this end, we use first-principles calculations within the framework of density-functional theory (DFT) along with experimental INS and Mass-resolved Neutron Spectroscopy (MANSE) data. INS provides a direct means of accessing the vibrational density-of-states (VDOS) and, as such, it is analogous and complementary to infrared and Raman techniques. Important merits and strengths of INS worthwhile recalling in the context of the present work include its outstanding sensitivity to hydrogen, the absence of selection rules, and the direct link to theoretical predictions.<sup>36,37</sup> MANSE, on the other hand, remains within the exclusive realm of neutron-scattering techniques as a unique probe of condensed-matter dynamics, and it is also of certain relevance to the physical and materials chemist. In brief, MANSE exploits the intense beams of epithermal neutrons in the electron-volt (eV) range available at last-generation accelerator-driven sources.<sup>36,38,39</sup> These are used to measure nuclear-recoil spectra in a *mass-selective* manner using time-of-flight (TOF) methods. These TOF data provide an experimental means of accessing in a model-independent manner nuclear-momentum distributions (NMDs), associated mean-kinetic energies, and underlying nuclear quantum effects (NQE).<sup>36,39–41</sup> Beyond fundamental phenomena such as NQEs in light and heavy water,<sup>42–44</sup> recent work has also extended the realm of applicability of MANSE to ordered and disordered lithium-containing

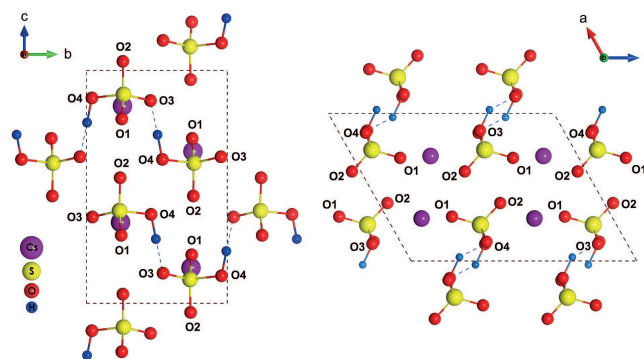


**Fig. 1** Structure of CsHSO<sub>4</sub> phase III showing the atomic labels adopted in the present study. These projections have been obtained with the VESTA program.<sup>52</sup>

compounds,<sup>45–47</sup> organic anti-ferroelectrics,<sup>48</sup> and hydrogen-storage nanostructured media.<sup>49</sup> Building upon these recent developments, we have performed DFT calculations to construct an extensive set of possible computational models of CsHSO<sub>4</sub> phase III over its range of stability at ambient pressure. We then validate their realm of applicability on the basis of their agreement with available experimental observables, including INS and MANSE data. For the first time, this comparison enables a detailed appraisal of the quantum contributions to nuclear motions in CsHSO<sub>4</sub> phase III, as well as provides a new conceptual framework for similar studies on other systems of both fundamental and practical interest.

## 2 Methodology

### 2.1 First-principles Calculations

Electronic-structure calculations were performed using the CASTEP 8.0<sup>50</sup> and CRYSTAL 14<sup>51</sup> DFT codes. In either case, they involved two sequential steps, taking as starting point the crystallographic structure of CsHSO<sub>4</sub> phase III previously reported by Itoh *et al.*<sup>7</sup> This structure is shown in Fig. 1. In a first step, we have used both plane-wave (PW) and linear-combination-of-atomic-orbitals (LCAO) DFT methodologies as currently implemented in CASTEP and CRYSTAL, respectively. The relative performance of PW-DFT and LCAO-DFT to describe CsHSO<sub>4</sub> phase III has been examined in detail, as described in the Electronic Supplementary Information (ESI). In what follows, we will focus on the PW-DFT calculations, which were found to provide a closer match to available experimental data. Following the above, a second step involved the calculation of phonon structure and associated INS and MANSE observables, as described in more detail further down below.

In the PW-DFT calculations, exchange and correlation were defined within the Generalized Gradient Approxima-

tion (GGA) and included the following functionals: the ‘standard’ Perdew-Burke-Ernzerhof (PBE),<sup>53,54</sup> its ‘hard’ revision by Hammer (rPBE),<sup>55</sup> and their ‘soft’ alternatives, namely, PBEsol<sup>56</sup> and Wu-Cohen (WC).<sup>57</sup> Core electrons were represented by Troullier-Martins norm-conserving pseudopotentials,<sup>58</sup> while electronic wave functions were expanded using a PW basis set with a kinetic-energy cutoff of 880 eV. The charge density was defined by multiplying the baseline size by a factor of four, the  $k$ -point grid was adjusted to maintain a constant spacing in reciprocal space of  $0.05 \text{ \AA}^{-1}$ , and the self-consistent-field energy was converged with a tolerance of  $10^{-12}$  eV/atom. Due to the well-known limitations of semi-local DFT approaches to describe van der Waals (vdW) interactions, the above functionals were also combined with the semiempirical dispersion corrections of Grimme (D2)<sup>59</sup> and Tkatchenko & Scheffler (TS).<sup>60</sup> Since the original D2 corrections did not include the Cs atom, we have used the parametrization introduced more recently by Zhang *et al.*<sup>61</sup> Global scaling factors for the damping functions, namely  $s_6$  (D2) and  $s_R$  (TS), were tuned so as to match the experimental unit-cell volume. To this end, the unit-cell volume of phase III was linearly extrapolated to 0 K using the most recent experimental data of Uda *et al.*<sup>28</sup> Global scaling parameters were varied systematically so as to minimise the deviation between the resulting unit-cell volume relative to experiment. In what follows, these reparametrized vdW corrections will be denoted as D2\* and TS\*.

Geometry optimization of ionic coordinates was performed both using a fixed unit cell or without constraints following full-cell relaxation at ambient pressure. Hellmann-Feynmann forces were minimised down to  $10^{-5}$  eV/atom and the associated stress components converged to within  $10^{-5}$  GPa. These (rather restrictive) convergence criteria were found to be necessary to attain a good convergence of phonon frequencies across the entire spectral range.

For insulating materials like CsHSO<sub>4</sub>, CASTEP supports dynamical-matrix calculations within the framework of density-functional perturbation theory.<sup>62–67</sup> Following this approach, optimised structures were used to calculate phonon-dispersion relations along the high-symmetry directions within the Brillouin zone (BZ). To this end, dynamical matrices were computed on a regular grid of wave-vectors  $q$  and Fourier interpolation was used to extend the computed grid to a desired set of 37  $q$ -points. Using calculated eigenfrequencies and eigenvectors, theoretical INS spectra were calculated using the aCLIMAX program.<sup>68,69</sup> As discussed in more depth in previous MANSE studies,<sup>45,47,49</sup> NMDs in a periodic solid are most conveniently described by considering the atom-projected VDOS (APVDOS) within the framework of the Gaussian approximation (GA). Within the spirit of the GA, the (experimentally accessible) Neutron Compton Profile (NCP) for nucleus  $n$  along the direction of the momentum

transfer  $\hat{q}$  adopts a Gaussian line shape, that is,

$$J(y; \hat{q}) = \frac{1}{\sqrt{2\pi\sigma^2}} \exp\left(-\frac{y^2}{2\sigma^2}\right) \quad (1)$$

where  $\sigma$  is the second moment (standard deviation) of the NCP with an associated mean kinetic energy  $E_k = \hbar^2\sigma^2/2M$  for a given nucleus of mass  $M$ ;  $y$  is the so-called West-scaling variable, defined as the the projection of the nuclear momentum  $\vec{p}$  onto  $\hat{q}$ . From these definitions, the square of the second moment of the NMD for a given nucleus  $n$  is obtained from the calculated phonon structure by performing the following sum over all modes<sup>47,49</sup>

$$\sigma_n(\hat{q})^2 = \frac{M_n}{N_q \hbar} \sum_q \sum_{\lambda} \times [\hat{q} \cdot e_n(\lambda, q)]^2 \frac{\omega(\lambda, q)}{2} \coth\left(\frac{\hbar\omega(\lambda, q)}{2k_B T}\right), \quad (2)$$

where  $\omega(\lambda, q)$  are calculated phonon frequencies and  $e_n(\lambda, q)$  are calculated polarization vectors associated with nucleus  $n$ . The summation in Eq. (2) runs over all  $q$  vectors contained in the first BZ ( $N_q$ ) and all phonon branches  $\lambda$  ( $N_\lambda$ ). Spherically averaged second moments are then obtained from Eq. (2) using<sup>70</sup>

$$\sigma^2 = \frac{1}{3} [\sigma(\hat{x})^2 + \sigma(\hat{y})^2 + \sigma(\hat{z})^2] \quad (3)$$

## 2.2 Neutron Spectroscopy

The high-resolution INS spectrum of CsHSO<sub>4</sub> phase III over the energy-transfer range 2–250 meV has been previously reported by Belushkin *et al.*<sup>14</sup> These data were collected at a temperature of 30 K using the TFXA spectrometer at the ISIS Facility (United Kingdom) and are freely available for download from the INS Database.<sup>71</sup> TFXA and its successor TOSCA are so-called inverted-geometry neutron spectrometers with a resolution comparable to infrared and Raman techniques across their entire spectral range.<sup>72</sup>

To complement the above INS data, additional MANSE measurements using epithermal neutrons were performed at 10 and 300 K on the VESUVIO spectrometer, also located at the ISIS Facility.<sup>73,74</sup> A total of 10.4 g of CsHSO<sub>4</sub> phase III was enclosed in an aluminium (Al) sachet of cross-sectional area  $3 \times 3 \text{ cm}^2$ , corresponding to a scattering power of ca. 9%. Additional details on the preparation and characterisation of this particular specimen can be found in the ESI.

The experimental and data-analysis protocol for these measurements is explained in more detail in previous MANSE works.<sup>45,48,75</sup> In brief, forward-scattering TOF data were measured at a total of 64 detectors over the angular range  $32\text{--}68^\circ$

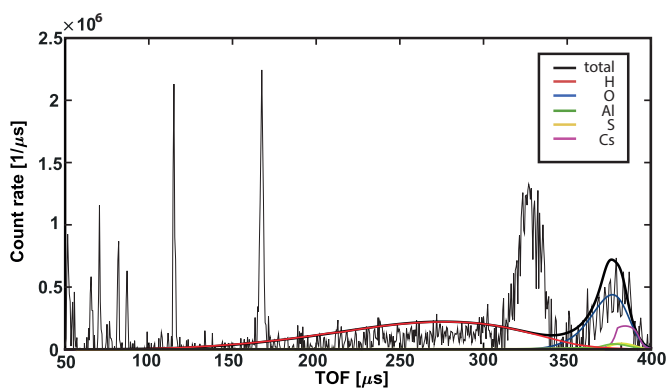


**Fig. 2** Angle-averaged, forward-scattering MANSE data for CsHSO<sub>4</sub> phase III at 10 K. In addition to the recoil data from all nuclides in the sample, the sharp features correspond to Cs neutron- $\gamma$  resonances, as described in the main text. The black trace corresponds to a fit of these experimental data using Eqs. (5) and (6). Other colours correspond to contributions from individual masses, see legend in the figure.

using a resonance-detector configuration.<sup>39</sup> The MANSE data arriving at a particular scattering angle  $\theta$  and TOF  $t$  are described as a linear sum of the distinct response from each element in the sample, namely,

$$C(\theta, t) = A \frac{E_0 I[E_0]}{q} \times \left[ \sum_M c_M J_M(x_M) \otimes R_M(x_M) \right], \quad (4)$$

where  $A$  is a proportionality constant,  $E_0$  and  $I[E_0]$  are the incident neutron energy and intensity, respectively, and  $q$  the momentum transfer. The NCP for a given mass  $M$  is of the form

$$J_M(x_M) = \frac{\exp(-x_M^2)}{\sqrt{2\pi\sigma_M^2}} \left[ 1 - \frac{k}{q} H_3(x_M) \right] \quad (5)$$

with  $x_M = (y_M)/(\sigma_M\sqrt{2})$ . As introduced earlier,  $\sigma_M$  is the standard deviation of the NMD for a given nuclide of mass  $M$ , and  $y$  is the West-scaling variable. The coefficients  $c_M$  are proportional to the product of the number density and neutron cross section of a given nuclide and have been fixed on the basis of the stoichiometry of CsHSO<sub>4</sub> and the relevant neutron-scattering cross sections.<sup>76</sup> Equation (4) also includes a convolution product ( $\otimes$ ) with a mass-dependent resolution function  $R_M$ . The second term in Eq. (5) accounts for deviations from the so-called impulse approximation. Within the harmonic approximation, these ‘final-state effects’ are related to the second moment of the NMD via  $k = \sigma\sqrt{2}/12$ .<sup>45</sup> Data

fitting was performed on a detector-by-detector basis as well as by using Cumulative Angle-Averaged Data (CAAD).<sup>45,48</sup> In the latter case, a CAAD is obtained by summing unit-area normalised TOF spectra, that is,

$$\text{CAAD} = \sum_{i=1}^N \frac{C(\theta_i, t)}{\int C(\theta_i, t) dt}. \quad (6)$$

The summation range  $N$  corresponds to a selection of detectors after exclusion of outliers and faulty detectors. In practice, this selection process involves the removal of individual TOF spectra that lead to reduced  $\langle \chi^2 \rangle$  values lower than 0.8 and higher than 1.2. This procedure was repeated until the exclusion of a given set of TOF spectra gave values of  $\sigma$  corresponding to the average value of fits over individual detectors, where the average was taken over the same range of TOF spectra. This data-analysis procedure leads to a more transparent assessment of the adequacy of a given NMD model in describing the experimental data.<sup>48</sup> As shown in Fig. 2, the presence of Cs atoms in the specimen led to the appearance of unwanted neutron- $\gamma$  resonances in the TOF data, characterised by sharp-features below 170  $\mu\text{sec}$  and over the interval 270-370  $\mu\text{sec}$ . This figure also illustrates that the inclusion of these features in the data analysis distorts the CAAD fits for H (see broad feature between 150 and 350  $\mu\text{sec}$ ), as well as underestimates recoil scattering from Al (see dark green line centered at  $\sim 375$   $\mu\text{sec}$ ). However, as the TOF associated with neutron- $\gamma$  resonances only depends on the incident neutron energy, these features are insensitive to scattering angle and, therefore, have been excluded from the MANSE analysis reported in this work.

## 3 Results and Discussion

### 3.1 Choice of DFT Functional

The structure of CsHSO<sub>4</sub> phase III shown in Fig. 1 is monoclinic (space group  $P2_1/c$ ,  $Z=4$ ) with  $a = 8.214(2)$   $\text{\AA}$ ,  $b = 5.809(2)$   $\text{\AA}$ ,  $c = 10.984(2)$   $\text{\AA}$ , and  $\beta = 119.39^\circ$ . This phase is characterised by the presence of well-defined zig-zag chains of hydrogen bonds along the crystallographic  $b$ -axis linking adjacent SO<sub>4</sub> tetrahedra. These hydrogen bonds are linear and strong, with a O $\cdots$ O distance of 2.55  $\text{\AA}$  at room temperature. Experimentally, it is known that the total cell volume of this phase at 296 K corresponds to 456.7  $\text{\AA}^3$ . Using the thermal expansion data of Uda *et al.*,<sup>28</sup> this value around room temperature extrapolates to 435  $\text{\AA}^3$  at 0 K. Figure 3 shows the results of a full-cell geometry optimisation for a series of PW-DFT functionals. A more detailed comparison including LCAO-DFT calculations can be found in the ESI, where it is shown that, for this particular system, neither meta-GGA nor solid-state-oriented hybrid functionals provide a noticeable improvement over the semi-local PW-DFT functionals

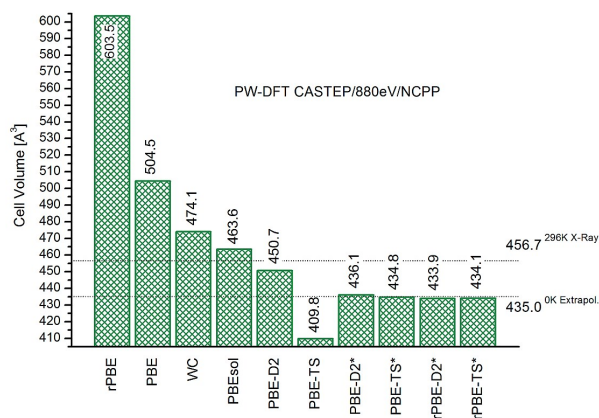


**Fig. 3** Calculated unit-cell volumes of CsHSO<sub>4</sub> phase III using PW-DFT. Dashed horizontal lines correspond to literature values, as discussed in the main text.

presented here. In agreement with previous studies on molecular solids,<sup>77</sup> these results show that the predicted cell volumes within the GGA follow the sequence ‘hard’ (rPBE) > ‘standard’ (PBE) > ‘soft’ (PBEsol, WC). Likewise, ‘soft’ GGA functionals seem to perform slightly better, although in all cases they remain considerably above our extrapolation of available experimental data to 0 K. A further compression of the unit-cell volume is obtained with vdW corrections, although PBE-D2 and PBE-TS still overestimate and underestimate the experimental value, respectively. A simple reparametrization of PBE-D2 ( $s_6=1.05$ , hereafter PBE-D2\*) and PBE-TS ( $s_R=1.05$ , hereafter PBE-TS\*) makes it possible to match the experimental unit-cell volume very accurately. We also note that a similar agreement can be obtained by introducing a greater weight for the dispersion correction to rPBE ( $s_6=1.75$ ,  $s_R=0.92$ ). This situation arises from the more repulsive nature of this functional, as evidenced at a quantitative level by the predictions of unit-cell volumes reported in Fig. 3.

On the basis of the above results, PBE-TS\* and rPBE-TS\* were chosen for a more detailed scrutiny, with optimised unit-cell parameters  $a = 7.994/8.050$  Å,  $b = 6.046/5.749$  Å,  $c = 11.192/10.401$  Å, and  $\beta = 126.52/115.60^\circ$  for PBE-TS\*/rPBE-TS\*. Figure 4 shows the electronic band structure across the BZ and associated density-of-states obtained from the PBE-TS\* and rPBE-TS\* calculations. These data display an electronic band-gap at the  $\Gamma$ -point of ca. 6 eV, a result fully consistent with the known insulating character of this material.

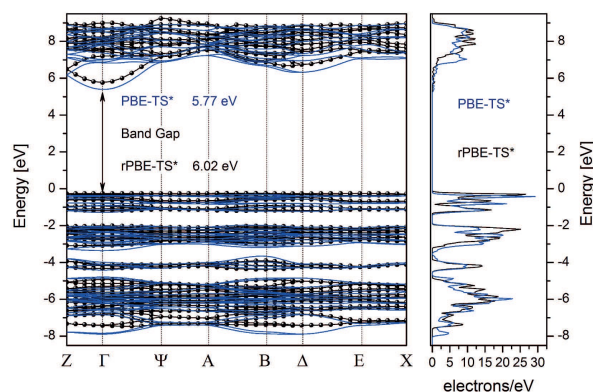


**Fig. 4** Calculated electronic band-structure (left) and density-of-states (right) for CsHSO<sub>4</sub> phase III.

### 3.2 Vibrational Dynamics

A comparison between experimental and calculated INS spectra is shown in Fig. 5. Although CsHSO<sub>4</sub> has been studied previously using optical techniques<sup>17,18</sup> and INS,<sup>2,14</sup> we note that no lattice-dynamics studies using first-principles calculations have been reported to date.

To facilitate spectroscopic assignments, INS spectra have been calculated by considering only fundamental transitions at the  $\Gamma$ -point, as well as via explicit calculation of mode dispersion across the BZ including overtones and combination bands up to tenth order (see solid and dotted lines in Fig. 5, respectively). Table 1 also reports a detailed comparison between experimental and calculated vibrational frequencies. We also provide approximate assignments of the main features in these data above 15 meV in terms of stretch modes ( $\nu$ ), in-plane ( $\delta$ ) and out-of-plane ( $\gamma$ ) deformations. A presentation of more extensive results using PW-DFT and LCAO-DFT may be found in the ESI. From these, we can conclude that PBE-TS\* and rPBE-TS\* provide the best agreement with experimental results for CsHSO<sub>4</sub> phase III. The explicit inclusion of vdW corrections in these two cases has certain advantages over the blind use of a fixed-cell scheme based on experimental values, as the latter approach gives rise to spurious internal stresses in the crystal structure and concomitant shifts in calculated vibrational frequencies. From the above comparison, we find a very good agreement between experimental and calculated INS spectra across the entire energy-transfer range. Although both PBE-TS\* and rPBE-TS\* provide a good description of the INS data, rPBE-TS\* is closer to observed mode energies.

The most prominent spectral features found in the experimental data may be discerned from direct inspection of fundamental transitions with no dispersion, as shown in Fig. 5.

**Table 1** Experimental and calculated INS frequencies for CsHSO<sub>4</sub> phase III. The rightmost column provides an approximate assignment of spectral features, as described in the main text. All numerical entries are in meV

Experiment	PBE-TS*	rPBE-TS*	Band Assignment
~347	298.2/291.1	347.4/344.7	$\nu$ -OH
~304	273.2/273.2	332.3/332.0	$\nu$ -OH
173.6	178.3/177.8	173.8/173.3	$\delta$ -OH
169.7	171.5/171.3	165.6/165.4	$\delta$ -OH
157.6	160.3/157.1/156.2/154.9	155.9/153.2/152.7/149.7	$\nu_{sym}$ -SO <sub>4</sub> + $\delta$ -OH
146.4	142.3/141.2/139.2/137.0	143.7/143.6/142.7/141.4	$\nu_{sym}$ -SO <sub>4</sub> + $\delta$ -OH
113.2	117.9/117.9	118.8/118.8	$\gamma$ -OH
108.5	116.7/116.4	112.1/112.1	$\gamma$ -OH
102.9	106.8/106.5/106.1/106.0	103.0/102.7/102.1/101.8	$\nu$ -SO <sub>H</sub>
76.2	77.7/77.3	75.5/75.0	$\delta$ -(H-O-S-O <sub>H</sub> )
75.0	74.8/74.1	73.1/72.9	$\delta$ -(O-S-O)
73.4	72.1/71.9/71.8/71.6	71.6/71.5/71.3/71.3	$\delta_{asym}$ -SO <sub>4</sub>
71.7	70.9/69.9/68.2/67.5	70.4/70.4/70.3/70.0	$\delta_{asym}$ -SO <sub>4</sub>
59.4	62.8	58.7	$\delta_{sym}$ -SO <sub>4</sub>
57.3	61.7	58.2	$\delta_{sym}$ -SO <sub>4</sub>
53.4	52.6/52.6	52.2/51.9	$\delta_{sym}$ -SO <sub>4</sub>
51.9	51.5/51.0/50.7/50.5	51.2/50.8/50.7/50.7	$\delta_{sym}$ -SO <sub>4</sub>
26.8	29.8/29.4	28.5/26.8	$\nu$ -(O...O)
25.7	28.7/28.3	26.0/25.4	$\nu$ -(O...O)
16.3	16.5/15.3	16.6/15.8	$\nu$ -(Cs...O)
14.7	15.3/14.7	15.2/15.1	$\gamma$ -(Cs...O...S)

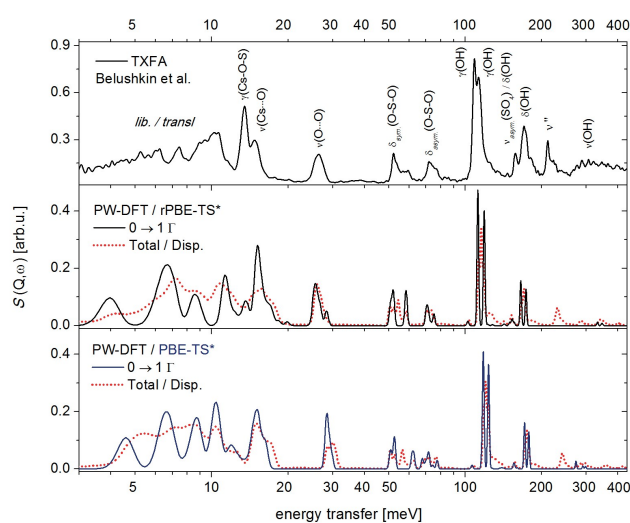


**Fig. 5** Experimental (top) and calculated (middle and bottom) INS spectra of CsHSO<sub>4</sub> phase III. For further details, see the main text.

Remaining (less intense) features in the INS data can be unequivocally assigned to overtone and combination bands. This result is further corroborated by the phonon-dispersion curves shown in Fig. 6. These data show little dispersion of specific mode energies above 20 meV, while the lattice region below this energy is clearly sensitive to these effects. A well-defined and intense doublet at ~15 meV is primarily associated with internal and external Cs...O stretchings mixed with  $\delta$ - and  $\gamma$ -Cs-O-S deformations, which are sensitive to the cell-structure and coordination of the Cs-O framework. Internal modes start with a rather sharp feature at 25 meV, associated with large-amplitude stretching modes of H-bridges. These low-energy HB stretching modes are also coupled to Cs-O-S deformations. We note that these considerations do not support the assignments proposed earlier by Belushkin *et al.*,<sup>14</sup> where this band was assigned to HSO<sub>4</sub><sup>-</sup> librations. Notwithstanding this discrepancy in interpretation, our assignments explain the downward shift of this band in phase II (caused by the elongation of H-bridges), as well as a well-known, pressure-induced blue-shift in phase V (arising from a shortening of the O...O distance).<sup>14</sup> These low-frequency bands are then followed by symmetric and antisymmetric SO<sub>4</sub> deformations centered at ~55 and ~73 meV. Above these energies, one finds internal vibrations associated with S-O bonds (~100 meV), as well as  $\delta$ - and  $\gamma$ -OH deformations associated with HBs and located at ~110 and ~170 meV. Contrary to what is found in phase II,<sup>14</sup> both of these modes split into two components, as clearly

confirmed by our first-principles calculations. Such a splitting comes from H $\cdots$ H contacts, which are induced by vibrations of B-symmetry. Transition to phase II gives rise to molecular reorientations in the  $b-c$  crystallographic plane. As a result, the distance between nearest-neighbour protons along the  $b$ -axis is longer than in phase III and, therefore, H-H correlations decrease. These dynamical-correlation effects are clearly manifested in the experimental spectrum for the  $\gamma$ -OH band, while the effect on  $\delta$ -OH modes is below the experimental resolution.<sup>14</sup>

In the case of  $\gamma$ -OH vibrations, the experimental results are consistently below computational predictions, an indication of significant anharmonicity for these particular modes. From the INS spectra, we also see that anharmonicity also reflects itself by the presence of a relatively intense overtone in the experimental data at  $\sim 210$  meV. This transition energy is significantly below harmonic predictions (see feature labeled  $\nu''$  in the experimental INS data shown in Fig. 5). We can quantify this deviation via recourse to a Dunham expansion of the vibrational energy  $E_\nu$  truncated to second order, namely,

$$E_\nu = \omega_e \left( \nu + \frac{1}{2} \right) - \omega_e x_e \left( \nu + \frac{1}{2} \right)^2 \quad (7)$$

where  $\nu$  is the vibrational quantum number and  $\omega_e$  and  $\omega_e x_e$  are harmonic and anharmonic constants, respectively. Defining the energies of the fundamental and overtone transitions as  $E_{10} = E_1 - E_0$  and  $E_{20} = E_2 - E_0$ , these two constants are given by  $\omega_e = 3E_{10} - E_{20}$  and  $\omega_e x_e = E_{10} - \frac{1}{2}E_{20}$ . Using experimental INS values, we obtain  $\omega_e = 117$  meV,  $\omega_e x_e = 3$  meV, and a ratio of anharmonic-to-harmonic constants  $x = \omega_e x_e / \omega_e = 0.026$ . This value of  $x$  is significantly lower than that found for phase II (0.0472). In view of the above, previous assignments of the band above 200 meV to exotic bi-phonon states in CsHSO<sub>4</sub> phase III are not supported by our lattice-dynamics calculations.<sup>14</sup>

The highest-lying vibrational modes corresponding to  $\nu$ -OH stretches are hardly discernable from the INS data, and they are clearly affected by recoil effects arising from the high momentum-transfers in this energy region. Dynamical H-H correlations also result in a large splitting of underlying A- and B-symmetry modes. Previous Raman studies<sup>17,18</sup> have located these modes over the range 300-350 meV. Computationally, their precise location is strongly dependent on unit-cell volume and choice of functional, with differences of up to 100 meV between ‘hard’ and ‘soft’ implementations of the GGA (see ESI). Somewhat surprisingly, the inclusion of vdW corrections was also found to be of relevance for these high-energy modes.

A more detailed description of our computational results may be found in the ESI, including computer animations of all normal modes of vibration in CsHSO<sub>4</sub> phase III.

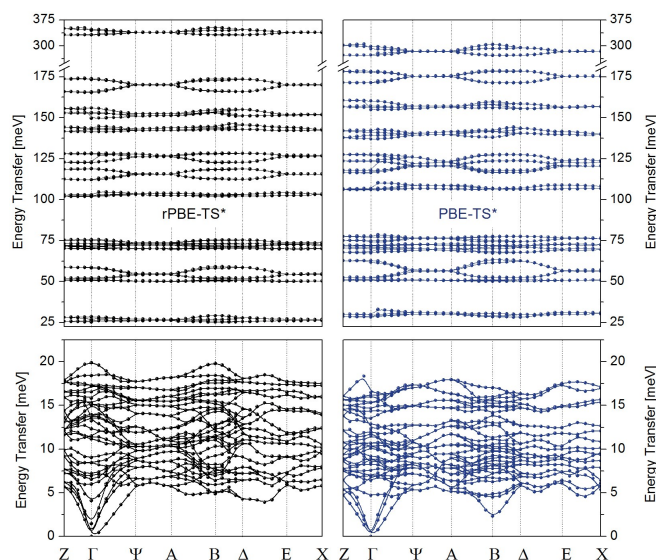


**Fig. 6** Calculated phonon-dispersion relations for CsHSO<sub>4</sub> phase III.

### 3.3 Nuclear Momentum Distributions

Within the harmonic approximation, APVDOSs derived from the phonon calculations provide a physical link between the INS data presented above and MANSE observables. To this end, Fig. 7 shows the total VDOS and APVDOSs obtained from the first-principles calculations for all atoms in the material. With the exception of the stretch modes above 250 meV associated with rapid vibrational motions of H and O atoms along the O-H bond, all remaining intensity lies within the first 200 meV. In this energy range, the H APVDOS is characterised by two distinct bands corresponding to motions transverse to the O-H direction. Likewise, the similarities between O and S APVDOSs reflect the pseudo-molecular character of the SO<sub>4</sub> moiety, whereas vibrational motions associated with the Cs atoms are restricted to energies below 25 meV, a region which also offers considerable overlap with slower O and S motions. From a chemical viewpoint, these results are consistent with the main structural features of CsHSO<sub>4</sub> phase III, which might be viewed as a binary Cs<sup>+</sup>SO<sub>4</sub><sup>2-</sup> lattice where SO<sub>4</sub><sup>2-</sup> units are closely interconnected via an arrangement of acceptor-donor HB pairs within the same SO<sub>4</sub><sup>2-</sup> ion. These structural motifs are most clearly seen via inspection of the crystallographic  $a-b$  plane shown in Fig. 1. This network of HB pairs translates into a manifest dispersive character of vibrational modes associated with proton motions, as evidenced by the phonon-dispersion relations shown in Fig. 6. These features are also in stark contrast with the arrangement of Cs<sup>+</sup> midway between two SO<sub>4</sub><sup>2-</sup> oxygen ions, evincing a much-less-pronounced chemical specificity associated with

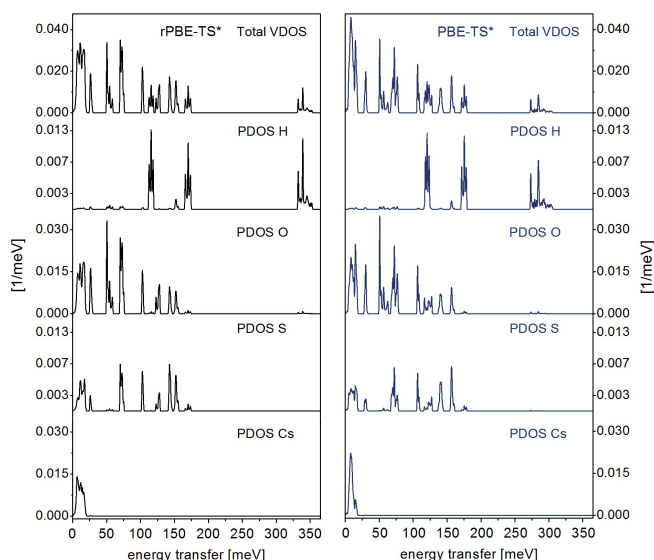


**Fig. 7** Total VDOS and individual APVDOSs for CsHSO<sub>4</sub> phase III, obtained from the rPBE-TS\* (left) and PBE-TS\* (right) calculations.

(predominantly ionic) Cs<sup>+</sup> ... SO<sub>4</sub><sup>2-</sup> interactions.

Building upon the insights gained so far in the analysis of the INS data and the APVDOSs, Tables 2 and 3 show rPBE-TS\* predictions for the second moment of the NMDs using Eqs. (2) and (3). These MANSE observables have been calculated along three orthogonal spatial directions where, for convenience,  $\hat{y}$  has been aligned parallel to the  $b$ -axis so that the  $\hat{x}-\hat{z}$  and crystallographic  $a-c$  planes coincide and  $\hat{z}$  is nearly parallel to the  $c$ -axis. In the coordinate system of the unit cell, the HB direction is roughly parallel to  $\vec{a} + \vec{c}$ . From these data, we note that both O atoms associated with HBs within a single SO<sub>4</sub> unit are distinguishable in terms of their NMDs (see O3 and O4 in Fig. 1). At  $T = 10$  K, the values of  $\sigma$  along the HB direction are 9.62 Å<sup>-1</sup> and 11.21 Å<sup>-1</sup> for O3 and O4, respectively. At 300 K, this difference becomes less distinct, namely, 12.00 Å<sup>-1</sup> and 12.96 Å<sup>-1</sup>. The two remaining oxygen atoms (O1 and O2) do not participate in hydrogen bonding. The calculated differences in  $\sigma$  for these two O species arise from a higher degree of localisation of O1 owing to its closer proximity to Cs. A similar trend towards a more isotropic NMD at the higher temperature is also observed for S, whereas Cs is essentially isotropic at both low and high temperatures.

Physically, a spatially averaged  $\sigma$  may be compared against the classical limit of a Maxwell-Boltzmann distribution at the same temperature  $T$  obeying  $\frac{3}{2}kT = \frac{3}{2}\frac{\hbar^2\sigma_{cl}^2}{M}$ . Using this classical relation between  $T$  and  $\sigma$ , we can write

$$\sigma_{cl} = \frac{\sqrt{MkT}}{\hbar} \quad (8)$$

As shown in Tables 2 and 3, these classical values provide a *lower* bound to the actual values of this observable, as chemical binding leads to an effective confinement of the atom under consideration and a concomitant increase in kinetic energy. Within the harmonic approximation, this excess kinetic energy strictly arises from the cumulative contribution of the zero-point energies (ZPEs) of *all* normal modes projected onto a given nucleus, as shown mathematically by Eq. (2). It is important to stress that MANSE provides direct experimental access to these kinetic energies irrespective of the specific nature (harmonic or not) of the underlying nuclear dynamics. From these considerations, we can also define a quantum-energy excess (QE) as the ratio of the squares of actual NMD widths relative to classical predictions, namely,

$$QE = \frac{\sigma^2}{\sigma_{cl}^2} = \frac{\hbar^2}{MkT}\sigma^2 \quad (9)$$

where, for clarity of presentation, we have made explicit the intrinsic (inverse) dependence of the QE on temperature  $T$  and nuclear mass  $M$ . Mathematically, both of these variables play an identical role in terms of approaching the classical limit (QE=1) as either of the two (or both) increases. To aid our discussion below, predicted QEs are also reported in Tables 2 and 3.

The computational predictions presented above can be compared with the MANSE measurements reported in Figs. 8 and 9. These figures show detector-summed MANSE data at 10 and 300 K along with their corresponding fits using the CAAD introduced in Section 2.2. As in earlier works, the NMD for the Al container has been described by a Gaussian NCP using literature values for the effective Debye temperatures at 10 K ( $\Theta=433$  K) and 300 K (390 K).<sup>45</sup> The experimental values for  $\sigma_H$  are 4.1±0.6 and 4.4±0.4 Å<sup>-1</sup> at 10 and 300 K, respectively. Within experimental uncertainties, these values compare quite favourably with our first-principles predictions, namely, 4.70 and 4.73 Å<sup>-1</sup>. The corresponding values of QE range from 100 at 10 K to 3.6 at ambient temperature, evincing the predominantly quantum character of the proton in CsHSO<sub>4</sub> phase III up to temperatures in close proximity to the reported transition to phase II at 330-370 K. In this regime,  $\sigma_H$  remains quite insensitive to temperature, as expected on physical grounds. This result is also consistent with the absence of phase III in the deuterated analogue CsDSO<sub>4</sub>, and suggests that differences in ZPEs lie at the heart of the well-known absence of phase III discussed earlier. Compared to other systems studied to date by MANSE, these values of  $\sigma_H$  are quite similar to those found for squaric acid at similar temperatures,<sup>48</sup> and significantly above those typical of ionic compounds like LiH<sup>45</sup> or molecular H<sub>2</sub> adsorbed in graphite-based intercalation compounds.<sup>49</sup> These relatively high values of  $\sigma_H$  are indicative of a strong binding environment for the proton, in spite of the well-known directionality of HB

**Table 2** First-principles predictions for MANSE observables at T=10 K. Nuclide labels in column 1 correspond to those shown in Fig. 1. Columns 2-4 correspond to projections along  $\hat{x}$ ,  $\hat{y}$ , and  $\hat{z}$ , whereas column 5 gives the isotropic value. The last two columns correspond to the classical limit of  $\sigma$  and QE, as discussed in the text. All values of  $\sigma$  are given in  $\text{\AA}^{-1}$

Nuclide	$\sigma(\hat{x})$	$\sigma(\hat{y})$	$\sigma(\hat{z})$	$\sigma$	$\sigma_{cl}$	QE
H	4.84	4.34	4.90	4.70	0.47	100
O1	8.43	8.17	14.16	10.62	1.82	34.1
O2	13.13	8.28	10.47	10.82	1.82	35.4
O3	10.77	11.74	9.69	10.77	1.82	35.0
O4	10.58	11.50	10.21	10.78	1.82	35.0
S	18.06	16.54	18.46	17.74	2.57	47.6
Cs	12.33	12.19	12.06	12.20	5.24	5.42

**Table 3** First-principles predictions for MANSE observables at T=300 K. Nuclide labels in column 1 correspond to those shown in Fig. 1. Columns 2-4 correspond to projections along  $\hat{x}$ ,  $\hat{y}$ , and  $\hat{z}$ , whereas column 5 gives the isotropic value. The last two columns correspond to the classical limit of  $\sigma$  and QE, as discussed in the text. All values of  $\sigma$  are given in  $\text{\AA}^{-1}$

Nuclide	$\sigma(\hat{x})$	$\sigma(\hat{y})$	$\sigma(\hat{z})$	$\sigma$	$\sigma_{cl}$	QE
H	4.87	4.37	4.93	4.73	2.50	3.6
O1	11.06	10.96	14.81	12.41	9.95	1.6
O2	14.13	10.97	12.40	12.57	9.95	1.6
O3	12.42	13.06	11.67	12.40	9.95	1.6
O4	12.42	12.74	12.13	12.45	9.95	1.6
S	19.64	18.53	20.02	19.41	14.10	1.9
Cs	28.35	28.85	28.85	28.80	28.80	1.0

motifs in these two systems. From a methodological viewpoint, these results bring to the fore the enticing possibility of using MANSE observables to establish a meaningful physico-chemical scale related to the chemical binding of hydrogen atoms in ordered and disordered media.

For heavier masses, the experimental MANSE data shown in Figs. 8 and 9 do not allow for an unambiguous isolation of the individual MANSE response of O, S, and Cs. Notwithstanding this limitation, the CAAD fits shown in this figure have been obtained by using the known stoichiometry of the material, neutron cross sections, and the calculated NMD widths reported in Tables 2 and 3. For either temperature, this procedure is capable of accounting for the experimental data satisfactorily in terms of the overall intensity and width of the observed recoil peak for the heavier masses, including the additional contributions from the Al container. Given the above, we can therefore conclude that our first-principles predictions are fully supported and consistent with the neutron-spectroscopic data at hand, both in the INS and MANSE regimes.

Further inspection of the QE values reported in Tables 2 and 3 reveals a number of important features. At 10 K, all nuclides are markedly quantum in nature by virtue of their intrinsic ZPEs, as evidenced by QE values well above unity. Although this is an expected result at these low temperatures, it is noteworthy that  $QE_S$  is ca. 40% higher than  $QE_O$ , the latter being a much-lighter species. For a similar confinement

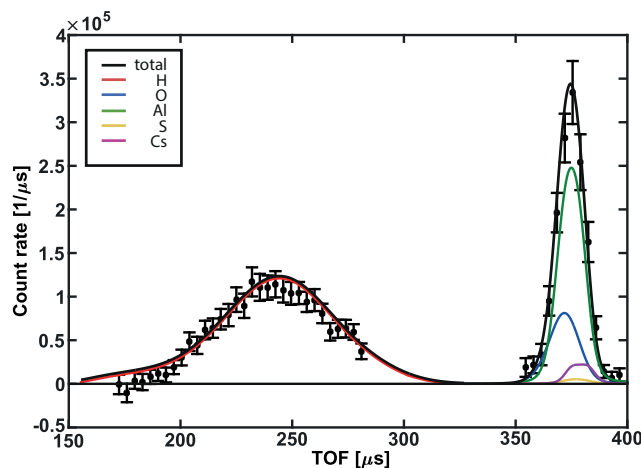


**Fig. 8** MANSE data and associated CAAD fits for  $\text{CsHSO}_4$  phase III at 10 K. For further details, see the main text.

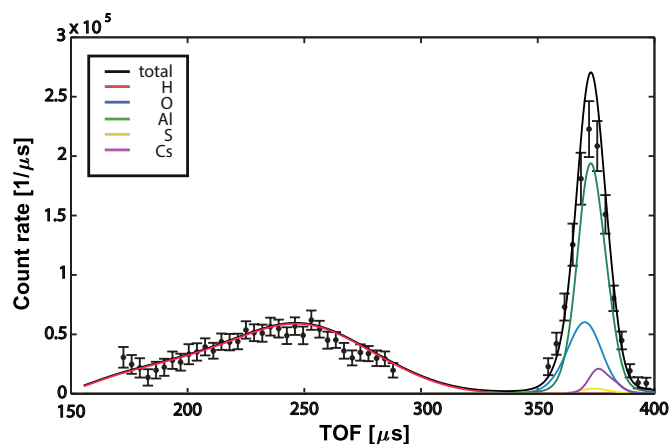


**Fig. 9** MANSE data and associated CAAD fits for CsHSO<sub>4</sub> phase III at 300 K. For further details, see the main text.

or binding potential, one would expect the reverse trend, and QE should scale approximately as the inverse of the ratio of their respective masses, leading to a decrease in  $QE_S$  relative to  $QE_O$  by a factor of  $M_S/M_O=32/16=2$ . This line of reasoning implies that S atoms have an associated kinetic energy ca. *three* times higher than expected if it were to experience the same interparticle potential as O. In physical terms, we can relate these results to the APVDOSs presented earlier in Fig. 7 as well as the structure shown in Fig. 1. Dynamically, the similarities found between S and O APVDOSs immediately imply a rough scaling of  $\sigma^2$  values by a factor of  $\sim 2$  in favour of S, as explicitly shown by Eq. (2). This observation is in qualitative agreement with the calculated ratio  $QE_S/QE_O \sim 1.40$ . It is also in line with the tetrahedral environment around the S atom compared with the peripheral location of the O atom in a given SO<sub>4</sub> unit. More surprisingly, the above differences between S and O are still evident at room temperature. In this case,  $QE_S=1.9$ , a value which is intermediate between H ( $QE_H=3.6$ ) and O ( $QE_O=1.6$ ). In either case, it is also important to stress that O and S atoms remain distinctly above the classical limit at 300 K. Last but not least, the manifest quantum behaviour seen for H, O, and S atoms is hardly of any consequence for Cs, whose QE varies between a modest value of 5.42 at 10 K and the classical limit of 1.0 at 300 K. This result is further reinforced by the APVDOSs presented earlier. For Cs, it remains peaked at a few meV and it is markedly different to those associated with other species in the material, a similar behaviour to what has been observed for alkali metals in graphite-intercalation compounds.<sup>49</sup>

Conversely, the data shown in Tables 2 and 3 also allow for quantitative estimates of the temperature where QE reaches unity for each nuclide in CsHSO<sub>4</sub> phase III. In increasing order, these temperatures are  $\sim 30$  K (Cs),  $\sim 500$  K (O),  $\sim 600$  K (S), and  $\sim 1000$  K (H). In the context of recent studies using

first-principles MD simulations,<sup>24–26</sup> our computational and MANSE results provide a strong indication that a purely classical description of nuclear motions in CsHSO<sub>4</sub> phase III over its temperature range of stability at ambient pressure should be questioned at the most fundamental level, as it only appears to apply to Cs at temperatures above  $\sim 30$  K.

## 4 Outlook

From a materials chemistry viewpoint, extensive state-of-the-art first-principles calculations and high-resolution neutron data have provided new insights into the properties of CsHSO<sub>4</sub> phase III. In particular, we have shown that available DFT functionals within the GGA can be used to describe the metastable phase of this solid acid, although such a description requires the explicit inclusion of vdW corrections. Likewise, lattice-dynamics calculations within the harmonic approximation validated via direct comparison with available experimental data provide a suitable starting point to understand vibrational motions at a quantitative level, as well as to reassess previous assignments and identify higher-order corrections, particularly those associated with anharmonic behaviour.

From a methodological viewpoint, we have also introduced a new conceptual framework linking computational predictions to INS and MANSE observables in order to explore the nuclear dynamics of individual atomic species. This methodology enables a detailed assessment of the quantum character of nuclear motions relative to classical predictions as a function of temperature via the use of the QE introduced in this work. In the specific case of CsHSO<sub>4</sub> phase III, this methodology provides strong indications that the (generally unquestioned) use of MD whereby atoms are treated as classical particles from the outset should be regarded as an approximation worthwhile revisiting in the context of known isotope effects and superionic conduction in this material at higher temperatures.

## 5 Acknowledgments

The authors gratefully acknowledge the UK Science & Technology Facilities Council for financial support and access to beam time at the ISIS Facility, as well as its e-Science Facility for access to supercomputing resources on the SCARF cluster at the Rutherford Appleton Laboratory. K.D. acknowledges partial support from the PL-Grid Infrastructure under grant *Solidstate2015-KD*, and the Ministry of Science and Higher Education of Poland for a mobility grant to fund his stay at the ISIS Facility in 2015.

## References

- 1 A. V. Belushkin, *Cryst. Rep.*, 1997, **42**, 501.

- 2 A. V. Belushkin, I. Natkaniec, N. M. Pakida, L. A. Shuvalov, and J. Wasicki, *J. Phys. C: Solid State Phys.*, 1987, **20**, 671.
- 3 A. M. Balagurov, A. V. Belushkin, I. D. Dutt, I. Natkaniec, M. Pakida, B. N. Savenko, L. A. Shuvalov and J. Wasicki, *Ferroelectrics*, 1985, **63**, 59.
- 4 A. I. Baranov, L. A. Shuvalov and N. M. Shchagina, *JETP Lett.*, 1982, **36**, 459.
- 5 S. M. Haile, D. A. Boysen, C. R. I. Chisholm and R. B. Merle, *Nature*, 2001, **410**, 910.
- 6 E. Ortiz, R. A. Vargas and B. Mellander, *J. Phys.: Condens. Matter*, 2006, **18**, 9561.
- 7 K. Itoh, T. Ukeda, T. Ozaki and E. Nakamura, *Acta Cryst. C*, 1990, **46**, 358.
- 8 K. Itoh, T. Ozaki and E. Nakamura, *Acta Cryst. B*, 1981, **37**, 1908.
- 9 P. Zetterström, A. V. Belushkin, R. L. McGreevy and A. L. Shuvalov, *Solid State Ionics*, 1999, **116**, 321.
- 10 A. V. Belushkin, R. L. McGreevy, P. Zetterstrom and A. L. Shuvalov, *Physica B*, 1998, **241-243**, 323.
- 11 A. V. Belushkin and W. I. F. David and R. M. Ibberson and L. A. Shuvalov, *Acta Cryst. B*, 1991, **47**, 161.
- 12 K. Kamazawa, M. Harada, Y. Ikedo, J. Sugiyama, M. Tyagi and Y. Matsuo, *J. Phys. Soc. Jpn.*, 2010, **79A**, 7.
- 13 A. V. Belushkin and C. J. Carlile and L. A. Shuvalov, *Ferroelectrics*, 1995, **167**, 21.
- 14 A. V. Belushkin, M. A. Adams, A. I. Kolesnikov, and L. A. Shuvalov, *J. Phys.: Condens. Matter*, 1994, **6**, 5823.
- 15 A. V. Belushkin and C. J. Carlile and L. A. Shuvalov, *J. Phys.: Condens. Matter*, 1992, **4**, 389.
- 16 H. Yamawaki, H. Fujihisa, M. Sakahita and K. Honda, *Phys. Rev. B*, 2007, **75**, 094111.
- 17 J. Baran and M. K. Marchewka, *J. Mol. Struct.*, 2002, **614**, 133.
- 18 M. Pham-Thi, Ph. Colombar, A. Novak, and R. Blinc, *J. Raman Spectrosc.*, 1987, **18**, 185.
- 19 D. Arcön, R. Blinc, J. Dolinšek and L. A. Shuvalov, *Phys. Rev. B*, 1997, **55**, 8961.
- 20 G. Lahajnar, R. Blinc, J. Dolinšek, D. Arčon and J. Slak, *Solid State Ionics*, 1997, **97**, 141.
- 21 R. Blinc, J. Dolinšek, G. Lahajnar, I. Zupančič, L. A. Shuvalov and A. I. Baranov, *Phys. Stat. Sol. B*, 1984, **123**, K83.
- 22 C. R. I. Chisholm, Y. H. Jan, S. M. Haile and W. A. Goddard III, *Phys. Rev. B*, 2005, **72**, 134103.
- 23 W. Münch, K. D. Kreuer, U. Traub and J. Maier, *Solid State Ionics*, 1995, **77**, 10.
- 24 B. C. Wood and N. Marzari, *Phys. Rev. B*, 2007, **76**, 134301.
- 25 X. Ke and I. Tanaka, *Phys. Rev. B*, 2004, **69**, 165114.
- 26 X. Ke and I. Tanaka, *Solid State Ionics*, 2004, **172**, 145.
- 27 C. R. I. Chisholm and S. M. Haile, *Mater. Res. Bull.*, 2000, **35**, 999.
- 28 T. Uda, D.A. Boysen, and S.M. Haile, *Solid State Ionics*, 2005, **176**, 127.
- 29 A. I. Baranov, *Cryst. Rep.*, 2003, **48**, 1012.
- 30 B. Baranowski, J. Lipkowski and A. Lundén, *J. Solid State Chem.*, 1995, **117**, 412.
- 31 A. Lundén and B. Baranowski and M. Friesel, *Ferroelectrics*, 1991, **124**, 103.
- 32 B. Baranowski, M. Friesel and A. Lundén, *Z. Naturforsch.*, 1987, **42a**, 565.
- 33 P. Colombar, M. Pham-Ti and A. Novak, *Solid State Ionics*, 1987, **24**, 193.
- 34 T. Steiner, *Angew. Chem. Int. Ed.*, 2002, **41**, 48.
- 35 A. R. Ubbelohde and K. J. Gallagher, *Acta Cryst.*, 1955, **8**, 71.
- 36 D. L. Price and F. Fernandez-Alonso, in *Neutron Scattering - Fundamentals*, ed. F. Fernandez-Alonso and D. L. Price, Academic Press, 2013, pp. 1 – 136.
- 37 M. R. Johnson and G. J. Kearley, in *Neutron Scattering - Fundamentals*, ed. F. Fernandez-Alonso and D. L. Price, Academic Press, 2013, pp. 415 – 469.
- 38 A. Pietropaolo and R. Senesi, *Phys. Rep.*, 2011, **508**, 45.
- 39 C. Andreani, D. Colognesi, J. Mayers, G. F. Reiter and R. Senesi, *Adv. Phys.*, 2005, **55**, 377.
- 40 A. G. Seel, R. Senesi and F. Fernandez-Alonso, *J. Phys. Conf. Ser.*, 2014, **571**, 012001.
- 41 A. G. Seel, M. Krzystyniak, R. Senesi and F. Fernandez-Alonso, *J. Phys. Conf. Ser.*, 2014, **571**, 012014.
- 42 A. Parmentier, J. J. Shephard, G. Romanelli, R. Senesi, C. G. Salzmann and C. Andreani, *J. Phys. Chem. Lett.*, 2015, **6**, 2038.
- 43 G. Romanelli, F. Fernandez-Alonso and C. Andreani, *J. Phys. Conf. Ser.*, 2014, **571**, 012003.
- 44 G. Romanelli, M. Ceriotti, D. E. Manolopoulos, C. Pantalei, R. Senesi and C. Andreani, *J. Phys. Chem. Lett.*, 2013, **4**, 3251.
- 45 M. Krzystyniak, S. Richards, A. G. Seel and F. Fernandez-Alonso, *Phys. Rev. B*, 2013, **88**, 184304.
- 46 A. G. Seel, M. Ceriotti, P. P. Edwards and J. Mayers, *J. Phys.: Condens. Matter*, 2012, **24**, 365401.
- 47 M. Krzystyniak and F. Fernandez-Alonso, *Phys. Rev. B*, 2011, **83**, 134305.
- 48 M. Krzystyniak, A. G. Seel, S. Richards, M. J. Gutmann and F. Fernandez-Alonso, *J. Phys. Conf. Ser.*, 2014, **571**, 012002.
- 49 M. Krzystyniak, M. A. Adams, A. Lovell, N. T. Skipper, S. M. Bennington, J. Mayers and F. Fernandez-Alonso, *Faraday Discuss.*, 2011, **151**, 171.
- 50 M. D. Segall, P. J. D. Lindan, M. J. Probert, C. J. Pickard, P. J. Hasnip, S. J. Clark and M. C. Payne, *J. Phys.: Condens. Matter*, 2002, **14**, 2717.
- 51 R. Dovesi, R. Orlando, A. Erba, C. M. Zicovich-Wilson, B. Civalleri, S. Casassa, L. Maschio, M. Ferrabone, M. De La Pierre, P. D'Arco, Y. Noel, M. Causa, M. Rerat, B. Kirtman, *Int. J. Quantum Chem.*, 2014, **114**, 1287.
- 52 K. Momma and F. Izumi, *J. Appl. Crystallogr.*, 2011, **44**, 1272.
- 53 M. E. J. Perdew, K. Burke, *Phys. Rev. Lett.*, 1997, **78**, 1396.
- 54 M. E. J. Perdew, K. Burke, *Phys. Rev. Lett.*, 1996, **77**, 3865.
- 55 B. Hammer, L. B. Hansen, and J. K. Nørskov, *Phys. Rev. B*, 1999, **59**, 7413.
- 56 J.P. Perdew, A. Ruzsinszky, G. I. Csonka, O. A. Vydrov, G. E. Scuseria, L. A. Constantin, X. Zhou, K. Burke, *Phys. Rev. Lett.*, 2008, **100**, 136406.
- 57 Z. Wu and R. E. Cohen, *Phys. Rev. B*, 2006, **73**, 235116.
- 58 N. Troullier and J. L. Martins, *Phys. Rev. B*, 1991, **43**, 1993.
- 59 S. Grimme, *J. Comput. Chem.*, 2006, **27**, 1787.
- 60 A. Tkatchenko and M. Scheffler, *Phys. Rev. Lett.*, 2009, **102**, 073005.
- 61 F. Zhang, J. D. Gale, B. P. Uberuaga, C. R. Stanek, and N. A. Marks, *Phys. Rev. B*, 2013, **88**, 054112.
- 62 K. Refson, S. J. Clark, and P. R. Tulip, *Phys. Rev. B*, 2006, **73**, 155114.
- 63 S. Baroni, A. Dal Corso, S. de Gironcoli, and P. Giannozzi, *Rev. Mod. Phys.*, 2001, **73**, 515.
- 64 X. Gonze, *Phys. Rev. B*, 1997, **55**, 10337.
- 65 X. Gonze, *Phys. Rev. A*, 1995, **52**, 1086.
- 66 X. Gonze, *Phys. Rev. A*, 1995, **52**, 1096.
- 67 S. Baroni, P. Giannozzi, and A. Testa, *Phys. Rev. Lett.*, 1987, **58**, 1861.
- 68 A. J. Ramirez-Cuesta, *Comput. Phys. Commun.*, 2004, **157**, 226.
- 69 D. Champion, J. Tomkinson, and G. Kearley, *Appl. Phys. A.*, 2002, **74**, S1302.
- 70 D. Colognesi, E. Degiorgi and E. Pace, *Physica B*, 2001, **293**, 317.
- 71 [www.isis.stfc.ac.uk/instruments/tosca/ins-database/](http://www.isis.stfc.ac.uk/instruments/tosca/ins-database/).
- 72 S.F. Parker, F. Fernandez-Alonso, A. J. Ramirez-Cuesta, J. Tomkinson, S. Rudic, R.S. Pinna, G. Gorini, and J. Fernández Castañón, *J. Phys. Conf. Ser.*, 2014, **554**, 012003.
- 73 A. G. Seel, M. Krzystyniak and F. Fernandez-Alonso, *J. Phys. Conf. Ser.*, 2014, **571**, 012006.

- 
- 74 G. Gorini, G. Festa and C. Andreani, *J. Phys. Conf. Ser.*, 2014, **571**, 012005.
- 75 S. Jackson, M. Krzystyniak, A. G. Seel, M. Gigg, S. E. Richards and F. Fernandez-Alonso, *J. Phys. Conf. Ser.*, 2014, **571**, 012009.
- 76 J. Dawidowski, J. R. Granada, J. R. Santisteban, F. Cantargi and L. A. Rodríguez Palomino, in *Neutron Scattering – Fundamentals*, ed. F. Fernandez-Alonso and D. L. Price, Academic Press, 2013, pp. 471 – 528.
- 77 K. Druzbicki, E. Mikuli, N. Pałka, S. Zalewski, and M. D. Ossowska-Chruściel, *J. Phys. Chem. B*, 2015, **119**, 1681.